In-situ Synthesized TiC/Ti-6Al-4V Composites by Elemental Powder Mixing and Spark Plasma Sintering: Microstructural Evolution and Mechanical Properties

Yuanmeng Wang[a], Ming Zhu [a,*], Longlong Dong [b, c, *], Guodong Sun [d], Wei Zhang [b], Hang Xue [d], Yongqing Fu [e], Ahmed Elmarakbi [e], Yusheng Zhang [b]

[a] School of Materials Science and Engineering, Xi'an University of Science and Technology, Xi'an 710054, PR China

[b] Advanced Materials Research Central, Northwest Institute for Nonferrous Metal Research, Xi'an 710016, PR China

[c] School of Materials Science and Engineering, Northeastern University, Shenyang 110819, PR China

[d] Xi'an Rare Metal Materials Institute Co., Ltd., Xi'an 710016, PR China

[e] Faculty of Engineering and Environment, Northumbria University, Newcastle upon Tyne, NE1 8ST, UK

Abstract: Titanium matrix composites synthesized using powder metallurgy methods have attracted significant attention due to their extraordinary mechanical properties. In this study, cost-effective and high-performance TiC/Ti-6Al-4V matrix composites were synthesized and characterized using a combined elemental powder mixing and spark plasma sintering method. Studies on the effect of graphene nanoplate (GNP) content on microstructures of Ti-6Al-4V matrix composites showed typical Widmanstatten structures without apparent pores and microcracks. The grain size of composites was

[*] Corresponding author:
E-mail address: donglong1027@163.com, mingzhu@xust.edu.cn

decreased significantly with the increase of GNP content, mainly due to the pinning effect of *in-situ* generated TiC particles at grain boundaries, which limited the rapid grain growth of the matrix. Mechanical test results showed that their yield strength and ultimate tensile strength were 889.0 MPa and 988.3 MPa, respectively, and their total fracture elongation was maintained at ~14.2%. GNPs/Ti-6Al-4V exhibited superior strength (e.g., yield and ultimate tensile strength of 1028.4 and 1121.6 MPa, which are 14.4% and 13.5% higher than those of the matrix) and maintained a good ductility of ~ 9.8% with only 0.1 wt% GNP addition. Carbon nanomaterial (such as graphene nanoplates) induced the precipitation of needle-like nano-secondary phases in trigeminal grain boundary β phases, which strengthened the β-Ti soft phase. The reinforced strength of the composite is mainly attributed to the grain refinement, secondary α phases precipitation strength and dislocations strengthening. This work provides a new methodology for fabrication of high-performance titanium matrix composites (TMCs) combination blended elemental powder metallurgy (BEPM) and sintering technology.

Keywords: Ti matrix composites, graphene, spark plasma sintering, mechanical properties, microstructure

1 Introduction

Ti-6Al-4V (TC4), a typical titanium alloy with both α and β phases, plays an important role in aerospace, automotive manufacturing, biomedicine fields, due to its excellent properties such as low density, high specific strength, corrosion resistance and good compatibility [1-3]. To enhance its mechanical properties, which are required for many applications, ceramic micro- or nano-phases (including TiB [4, 5], TiC [5, 6], B_4C

[7] and SiC [8] etc.) reinforced titanium matrix composites (TMCs) have recently attracted extensive attention. There are generally two types of fabrication methods for TMCs, i.e. *in-situ* and *ex-situ* ones. Compared with the *ex-situ* methods, *in-situ* ceramic phases formed at interfaces can effectively improve mechanical properties due to their good interface binding and wettability within the Ti matrix [9, 10].

Graphene, with its excellent mechanical properties such as high elastic modulus (1 TPa) and high fracture strength (130 GPa) [11], has been considered as an effective reinforcement in aluminum [12], magnesium [13], copper [14] and titanium [15-20] and their alloys to improve the mechanical properties of these metal matrix. Previously, we fabricated graphene reinforced TMCs using a combined powder metallurgy and hot rolling process, and the composites showed a significant increase in strength with acceptable elongation [21-24]. Zhang et al. [25] used polyvinyl alcohol chemical modification and spark plasma sintering (SPS) processes to fabricate 3D-network architectures of graphene reinforced TMCs, which achieved a good balance of strength and ductility. Recently, other methods (such as 3D-printing [26-29], sintering-free process [30]) have also been used for fabricating nanocarbon/Ti composites. Zhou et al. [26, 27] coated the surface of Ti-6Al-4V powders with acid-treated carbon nanotubes (CNTs) or graphene oxides using an electrostatic self-assembly method without changing the sphericity of the powders. High-performance TiC/Ti-6Al-4V composite was synthesized using a 3D-printing laser powder bed fusion technology, and the morphology of TiC was found to change from nanorods to microspheres and then to dendrites with an increase of CNT contents. Liu et al. [30] developed a sintering-free process combining cold compaction and hot extrusion to fabricate CNTs/Ti composites, and their ultimate tensile strength was 1262 MPa and the elongation was only 4.3%.

Although graphene/Ti-6Al-4V composites fabricated using the powder metallurgy

exhibited excellent mechanical properties, Ti-6Al-4V powders used in these previous studies are costly due to their special powder manufacturing technology (e.g., plasma rotation electrode process) [31]. Therefore, it becomes crucial to develop a low-cost process for these TMCs. In general, blended elemental powder metallurgy (BEPM) has been considered an effective and cost-effective method [32] for fabricating TMCs with desirable microstructures and characteristics [33]. It was reported that Ti-6Al-4V alloy was fabricated using TiH_2 powders and 60Al-40V intermediate alloy powders, but TiH_2 powders were needed to be processed in a high vacuum [34]. Yang et al. [35] fabricated Ti-6Al-4V powder using the BEPM method from a mixture of hydride–dehydride (HDH) Ti powder, Al powder and 35Al-65V alloy powder, and then the mixed powder was cold pressed, sintered and hot extruded to produce alloy rods. The fabricated samples showed comparable tensile properties to those of Ti-6Al-4V cast alloys, and the ultimate tensile strength, yield strength and elongation to fracture reached about 1272 MPa, 1200 MPa and 10%, respectively [35]. However, its preparation process is complicated.

Although the BEPM fabricated Ti-6Al-4V alloys exhibit excellent tensile properties and the base powders used (e.g., TiH_2 or HDH Ti) are cheap, the pre-sintered specimens often present substantial residual voids in the Ti alloy matrix. Therefore, post-processing (e.g., hot extrusion [34, 35] or second sintering [33]) is often required to increase their density. Additionally, due to the low fluidity of TiH_2 and HDH Ti powders, it is difficult to disperse the nanocarbon sources uniformly in the process of fabricating titanium matrix composites, which limits their applications in TMCs [36]. In view of the above issues, this study provides the possibility of using the BEPM to fabricate cost-effective TMCs without secondary processing. Pure titanium powder is used as the base powder, different from TiH_2 powder, which avoids the dehydrogenation

process under an extremely high vacuum. Therefore, this is an easy-to-process and cost-effective method for fabricating titanium matrix composites. So far, studies on fabricating *in-situ* TiC/Ti-6Al-4V composites by BEPM and SPS from pure titanium powders have not been widely reported.

Herein, a combined BEPM and SPS method was used to *in-situ* synthesize TiC/Ti-6Al-4V composites. Graphene with different contents (0, 0.1, 0.2 wt.%) and pure titanium powders and Al-V master alloy powders were mixed synergistically. Then the composites were synthesized using the SPS process. Microstructure and mechanical properties of fabricated composites were investigated, from which strengthening and fracture mechanisms were identified.

2 Materials and methods

2.1 Starting materials

Chemical compositions of Ti and 60Al-40V powders in this work are listed in **Table 1**. Titanium powder (15-53 μm with 99.9% purity) was purchased from Xi'an SinoEuro Materials Technologies Co., Ltd., China. The particle size of pure Ti powder is widely distributed and the average particle size is 28.88 ± 5 μm (as shown in **Figures 1a-a$_1$**), which is beneficial for sintering neck formation during sintering and enabling complete powder densification. Scanning electron microscope (SEM) morphologies of the 60Al-40V alloy powders are shown in **Figures 1(b-b$_1$)** with uneven shapes. These powders were ball-milled for 0.5 h at a speed of 300 r/min and sieved to reduce particle size. Graphene nanoplates (GNPs) were purchased from Nanjing XFNANO Technology Co., Ltd., China. The SEM images (**Figures 1c-c$_1$**) and transmission electron microscope (TEM) images (**Figure 1d**) of GNPs show large-scale, thin-layered and wrinkled microstructures (purity > 98 wt.%, average size 1–3 μm in diameter and

thickness 1–5 nm). However, there are many nanoscale defects existed on the edges of GNPs, as marked by arrows in **Figure 1d$_1$**.

Table 1. Chemical compositions of Ti and the 60Al-40V powder. (wt.%)

Materials	Al	V	Fe	C	N	O	H	Ti
Ti	-	-	0.157	0.006	0.002	0.16	0.003	Bal.
60Al-40V	58.64	40.31	0.13	0.010	0.022	0.27	0.012	-

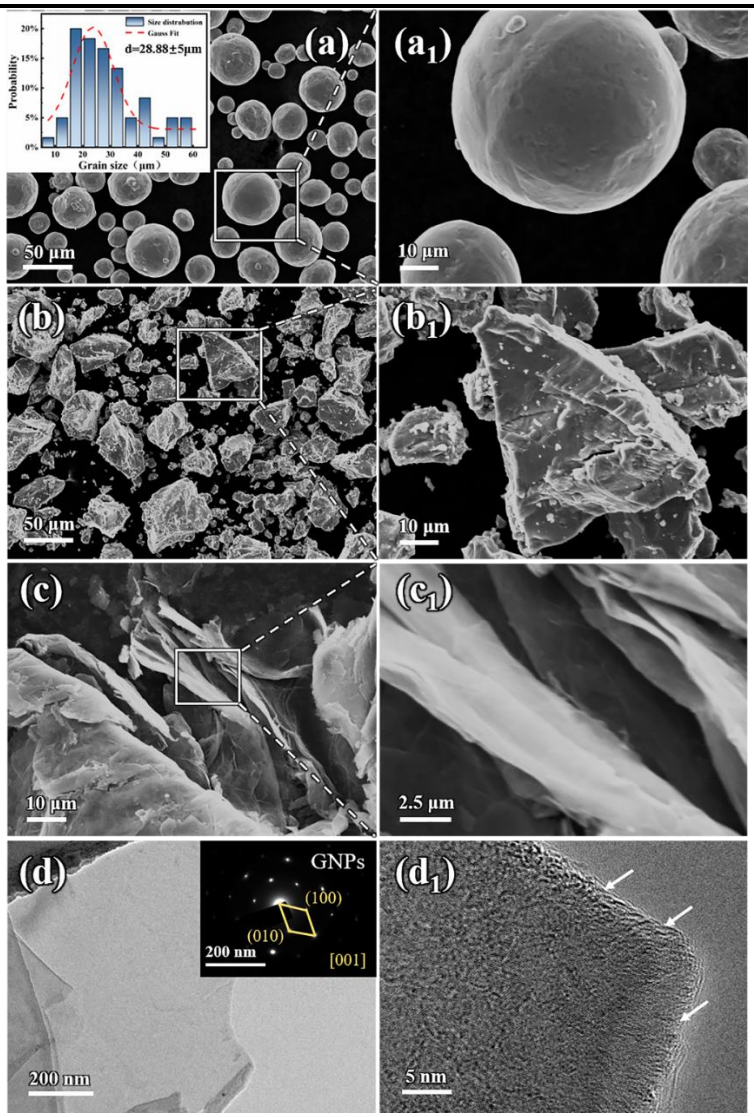

Figure 1. SEM images of (a-a$_1$) pure Ti powder, (b-b$_1$) 60Al-40V and (c-c$_1$) GNPs, respectively; (d) TEM image (inset the select electron diffraction pattern) and (d$_1$) high resolution TEM image of GNPs.

2.2 Preparation of Ti-6Al-4V and GNPs/Ti-6Al-4V powders/composites

Ti powders, fragmentized 60Al-40V powders and GNPs were thoroughly mixed using planetary ball milling (QM-3SP2, Nanda Instrument Plant, Nanjing, China) under argon atmosphere to prevent the oxidation of Ti powders. Ti and 60Al-40V powders were proportionally mixed according to their nominal compositions and then ball-milled at a speed of 300 r/min for 5 h to obtain Ti-6Al-4V alloyed powders. Meanwhile, GNPs/Ti-6Al-4V composite powders were obtained by ball milling Ti, 60Al-40V and GNPs at a speed of 200 r/min for 5 h, and then at 300 r/min for 4 h. The ball-powder ratio was 3:1 during ball milling for both mixture powders.

SPS method was used in the present work, and the overall process flow for fabricating GNPs/Ti-6Al-4V composites is illustrated in **Figure 2**. The furnace was pumped to 10^{-2}-10^{-3} Pa and heated to 1050 °C at 100 °C/min, which was monitored using an infrared thermometer, and then held for 5 min under the pressure of 45 MPa.

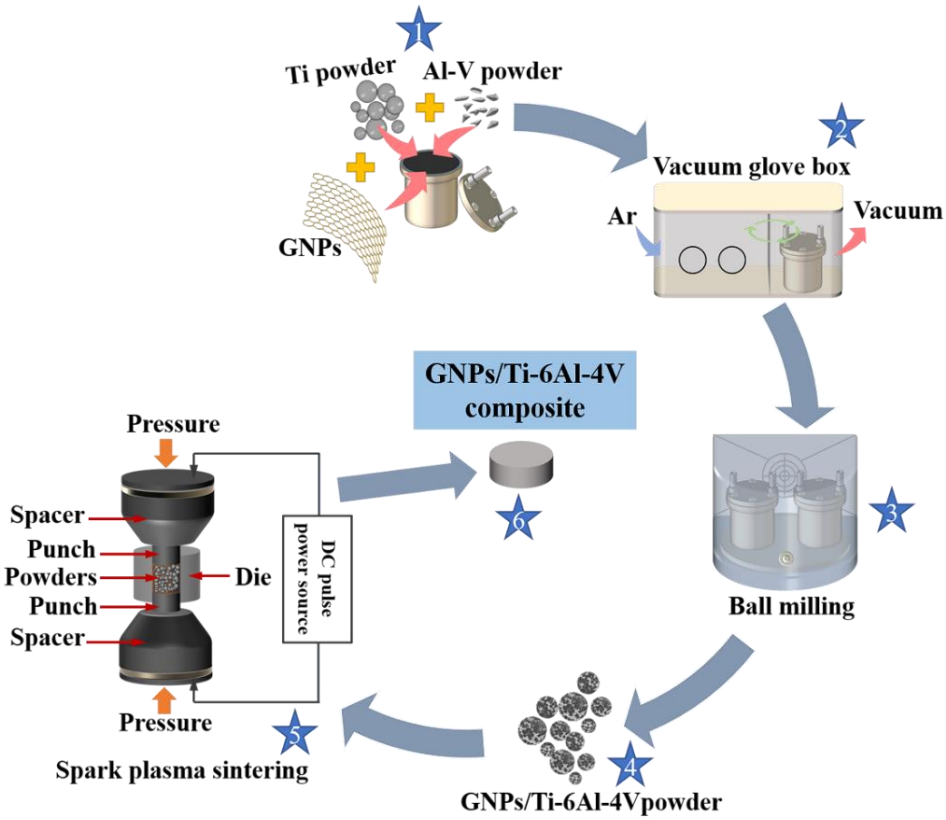

Figure 2. Preparation process of GNPs/Ti-6Al-4V composite.

2.3 Microstructure and property analysis

Crystalline phases of the composites were characterized by X-ray diffraction (XRD, Bruker D8 ADVANCE). Scanning electron microscope (SEM, EM-30AX^{+}) equipped with energy dispersive spectrometer (EDS) was used to characterize the microstructures and fracture morphology of mixed powders and as-sintered composites. To estimate the average grain size of the composites, we measured the values along different directions of each grain and obtained an average value from those of a large number (more than 50) of grains [24]. Before SEM characterization, as-sintered samples were polished with sandpapers and then with aluminum oxide solutions until the surface of the samples showed no major defects or scratches. They were then etched using a Kroll solution (1 mL HF: 3 mL HNO_3: 10 mL H_2O). Meanwhile, the microstructures of the sintered composites were also analyzed using a high-resolution transmission electron microscope (HR-TEM, FEI Tecnai F20) together with the selected area electron diffraction (SAED) method.

Densities of sintered composites were measured using the Archimedes method. The relative densities of all samples are ~98%, indicating that the SPS process can efficiently densify composites (**Figure 8c**). The hardness of the sintered sample was obtained from 10 different positions with a normal load of 10 N and a loading time of 15 s by using a Vickers microhardness tester (MVS-1000IMT2), and the average value was obtained. Tensile properties of the sintered TMCs were tested at room temperature using an UTM5105X universal testing machine with a strain rate of 1 mm/min in accordance with GB/T 228.1-2010. Dog bone-shaped specimens with a gauge length of 50 mm and a gauge width of 11 mm were prepared using an electro-discharge machining technique. At least three samples were tested to obtain average tensile

properties.

3. Results and discussions

3.1 Morphology of mixed powders

Compared with the original spherical Ti powder shown in **Figures 1(a)~ (a_1)**, the composites powders exhibit slightly deformed shapes and rough particulate surface features (**Figures 3a-c_1**) after ball milling. EDS mapping images shown in **Figures 3(c_2-c_5)** demonstrate that Al, V and C elements are uniformly distributed on the surfaces of the composite powders, revealing that Al-V particles and GNPs were coated on the surface of Ti powders.

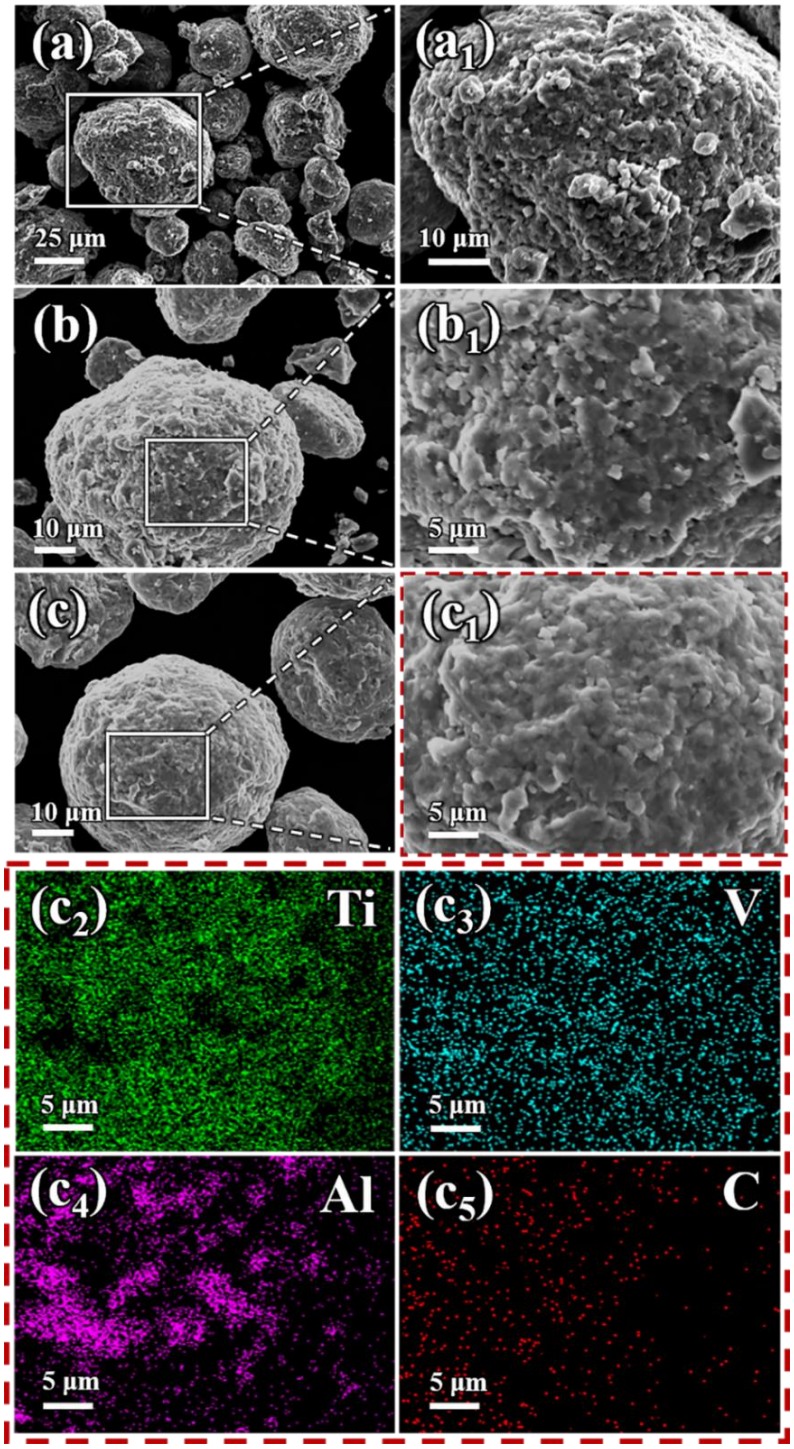

Figure 3. SEM images of blended powder: (a-a_1) Ti-6Al-4V; (b-b_1) 0.1 wt.% GNPs/Ti-6Al-4V; (c-c_5) 0.2 wt.% GNPs/Ti-6Al-4V and the corresponding EDS mapping results of Ti, V, Al and C elements.

3.2 Phase composition and microstructure of the composites

As shown in **Figure 4**, peaks corresponding to hexagonal close-packed (HCP) α-Ti and body-centered cubic (BCC) β-Ti can be detected in Ti-6Al-4V alloy and GNPs/Ti-6Al-4V composites. Furthermore, there is a weak (111) TiC peak in the 0.2 wt.% GNPs/Ti-6Al-4V composite. GNPs inevitably react with the matrix to form carbides because the carbon content exceeds its solution limit (0.05 wt.%) in the matrix [37]. However, diffraction peaks corresponding to graphene or other carbides are not detected by XRD, because of the low content of GNPs in the composites. It is depleted by the reaction of Ti with C [38], which will be discussed further later.

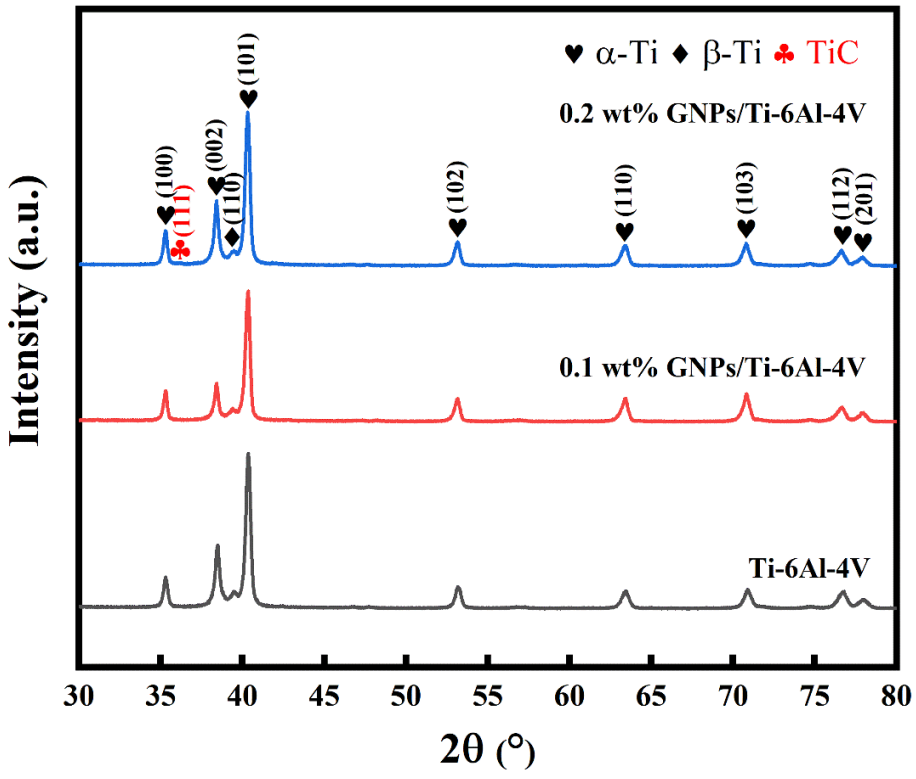

Figure 4. XRD analysis of sintered composites

Figure 5 shows SEM images of Ti-6Al-4V composites with various GNPs contents. All the samples are dense without apparent pores and microcracks after SPS processing at 1050 °C. The matrix exhibits a typical Widmanstatten microstructure because the sintering temperature was higher than the phase transition temperature of

Ti-6Al-4V alloy [39]. Whereas small amounts of TiC particles were observed in composites, as shown in **Figures 5(b)** and 5**(c)**, indicating the interfacial reactions between graphene and the Ti-6Al-4V powder during the sintering process. As shown in **Figures 5(a_2-c_2)**, the estimated average grain sizes for composites of 0.1 wt.% GNPs/Ti-6Al-4V and 0.2 wt.% GNPs/Ti-6Al-4V are 62.81 μm and 45.78 μm, respectively, both of which are smaller than Ti-6Al-4V alloy (68.76 μm). This could be explained by a grain refinement effect of TiC particles formed during the sintering on the matrix [40]. This grain refinement effect is more significant for the composites with 0.2 wt.% GNPs, which is mainly due to the formation of more TiC particles in the matrix (with an average size of 1-3 μm). The theoretical weight percentages of formed TiC particles in 0.1 wt.% GNPs/Ti-6Al-4V and 0.2 wt.% GNPs/Ti-6Al-4V are 0.5 wt.% and 1 wt.%, respectively.

To investigate the thermodynamics of carburizing reactions between matrix and GNPs during the sintering process, the Gibbs free energy (ΔG) and reaction formation enthalpy (ΔH) of possible carbide formation at the interfaces were calculated. Carburizing reactions that could occur during the sintering process are listed as follows [41-43]:

$$\mathrm{Ti(s) + C(s) = TiC(s)} \quad (1)$$

$$\mathrm{4Al(s) + 3C(s) = Al_4C_3(s)} \quad (2)$$

$$\mathrm{V(s) + C(s) = VC(s)} \quad (3)$$

The corresponding Gibbs free energy (ΔG, KJ/mol) and formation enthalpy (ΔH, KJ/mol) of these reactions can be obtained using the following equations [44, 45]:

$$\Delta G = \Delta G^{\theta} + RT \ln Q \quad (4)$$

$$\Delta H = \Delta G + T\,\Delta S \quad (5)$$

where R is the reaction constant, T is the reaction temperature (K), Q is the heat loss

energy at T (kJ), and ΔS is the reaction entropy (kJ/K/mol) [44]. The calculated results for ΔG and ΔH are shown in **Figures 5(d)** and **(e)**, respectively. Since the sintering process was performed at a temperature of 1050 ℃, we ranked the ΔG and ΔH values for these carbide formation according to the following order: $\Delta G_{\mathrm{VC}} > \Delta G_{\mathrm{Al_4C_3}} > \Delta G_{\mathrm{TiC}}$, and $\Delta H_{\mathrm{VC}} > \Delta H_{\mathrm{TiC}} > \Delta H_{\mathrm{Al_4C_3}}$. The negative result of Gibbs free energy indicates the thermodynamic feasibility of TiC formation, and the negative enthalpy values obtained indicate that the formation of TiC is an exothermic reaction, thus revealing that Ti and C reactions easily occur during the sintering process [46, 47]. Since the Gibbs free energy of TiC is the lowest, it reveals that the Ti and C reactions occur preferentially during the sintering process. Moreover, the content of graphene added in the experiment is very small, so Al and V have no chance to react with graphene to form carbides, resulting in the formation of Al-rich and V-rich regions.

From the bright-field TEM image shown in **Figure 6a**, some dislocations are distributed within the grains, which could be beneficial to improve the mechanical properties of titanium alloy [48]. EDS mapping shown in **Figures 6(a_1-a_3)** reveal the distribution of α-Ti and β-Ti, and SAED patterns (**Figures 6b_1** and **6c_1**) of their corresponding areas further confirm the existence of both α and β phases, revealing that Ti, Al and V elements fully diffused to form a typical α+β biphasic structure. Interstitial carbon is an effective strengthening element and carbon atoms are preferably confined to α-Ti in an α + β titanium alloy [21]. **Figure 6(d)** displays a dark-field TEM image of 0.2 wt.% GNPs/Ti-6Al-4V composite, and the bright bulge pattern in α-Ti was identified as face-centered cubic TiC according to the SAED pattern (see the inset image) and the corresponding EDS mapping image **(Figures 6d_1-d_4)**. The crystal structure leads to the isotropic growth of TiC, so the mechanical properties in all directions are the same, which is beneficial for the properties of *in-situ* formed TiC

reinforced Ti-6Al-4V matrix [49]. It is worth noting that there are many dislocations around TiC particles (shown in **Figure S1**) which were resulted from the inhibition of dislocation movement and accumulation of dislocations near TiC, thus enhancing the mechanical properties of composites [50, 51]. Furthermore, GNPs as a carbon source would induce defects in α-Ti phases near the TiC interface that trigger more dislocations [52]. The large number of interfacial dislocations also means that there are large internal stresses between TiC and matrix [51-53]. **Figure 6e** shows a scanning transmission electron microscopy (STEM) image of the phase boundary region of the 0.2 wt.% GNPs/Ti-6Al-4V composite. Some secondary α-Ti (α'') can be distinguished in β-Ti, which has been demonstrated to strengthen the β-Ti [32], and the shapes of these secondary α-Ti phases can be clearly defined in the bright-field image (**Figure 6f**). **Figure 6g** shows the HRTEM image of the corresponding area in **Figure 6f**, and the secondary α-Ti formed in β-Ti phases can be further confirmed by the SAED patterns (insert images) obtained using the Fast Foourier Transform (FFT) method.

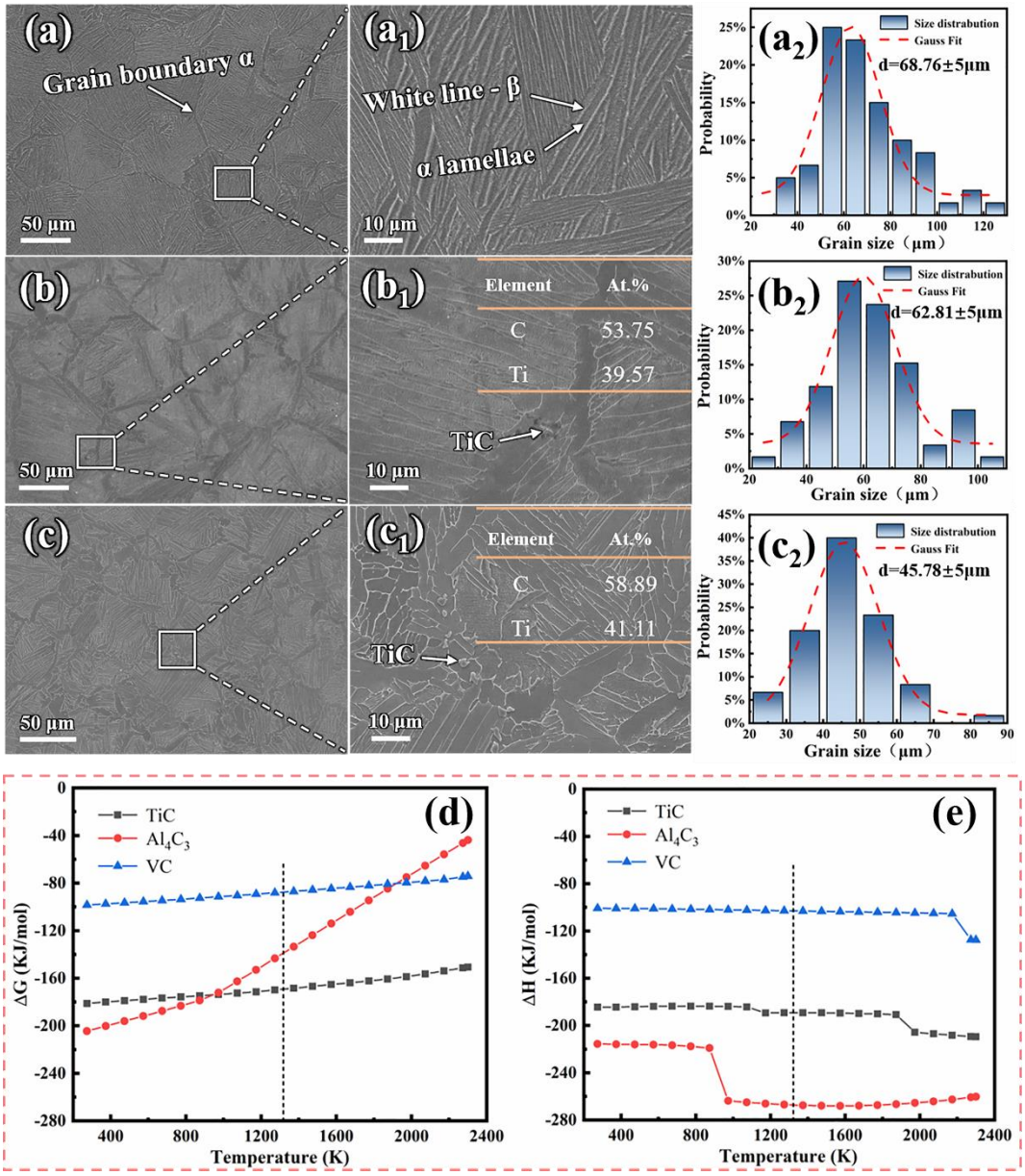

Figure 5. SEM images of GNPs/Ti-6Al-4V composites reinforced with various GNPs contents: (a) Ti-6Al-4V alloy, (b) 0.1 wt.% GNPs/Ti-6Al-4V composites, (c) 0.2 wt.% GNPs/Ti-6Al-4V composites, (a_1-c_1) are magnified views of (a-c), respectively; (a_2-c_2) Grain size distribution of Ti-6Al-4V alloy and GNPs/Ti-6Al-4V composites, respectively. (d) and (e) are the comparison of Gibbs free energy (ΔG) and reaction formation enthalpy (ΔH) of carbides based on HSC chemistry soft 6.0 calculations, respectively.

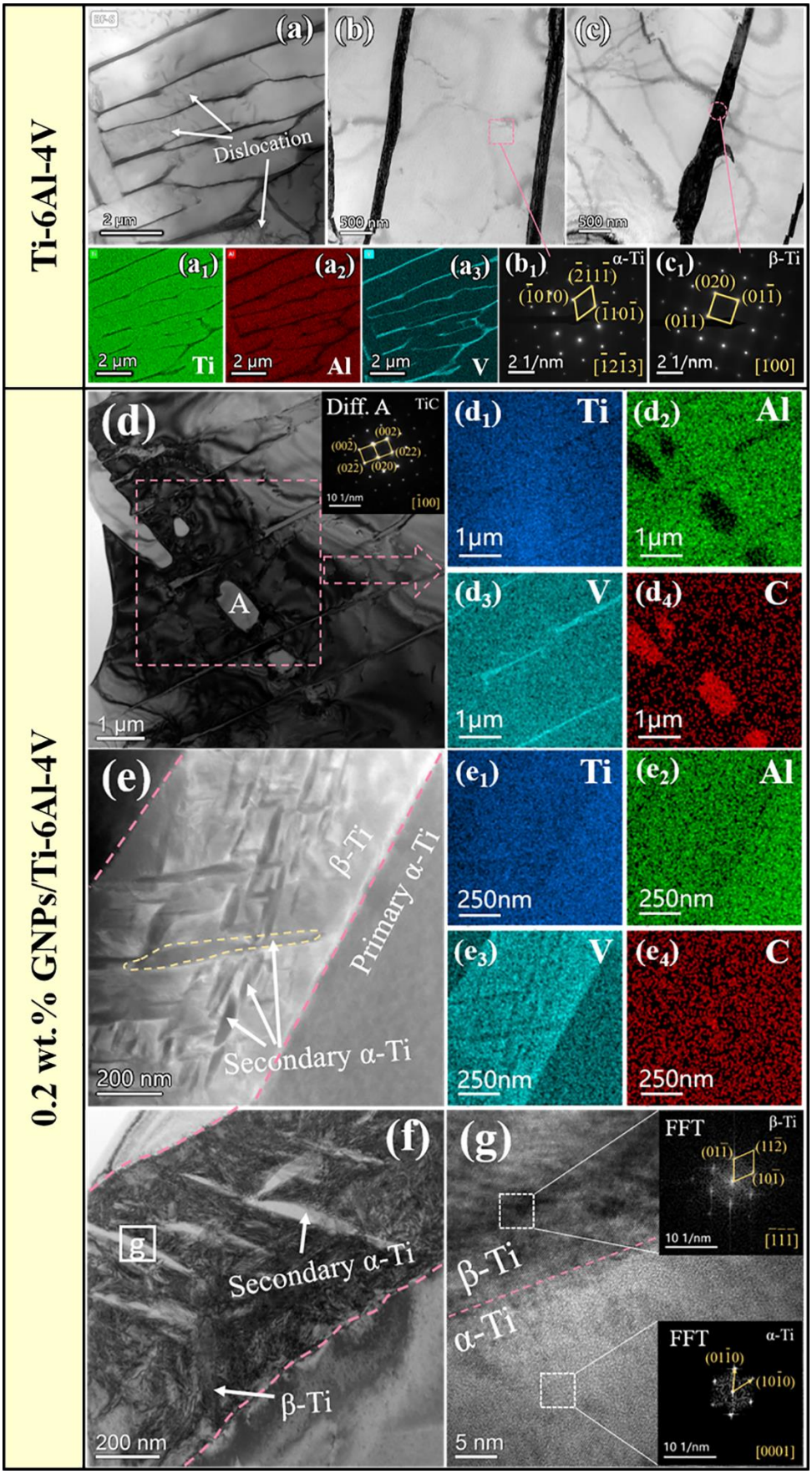

Figure 6. TEM images of Ti-6Al-4V alloy and 0.2 wt.% GNPs/Ti-6Al-4V composites:

(a), (b) and (c) are the bright-field images of Ti-6Al-4V alloy at different positions, and EDS mapping and SAED pattern of the corresponding area. (d) Dark-field of 0.2 wt.% GNPs/ Ti-6Al-4V composites and the SAED pattern marking the location are inserted. (d_1), (d_2), (d_3) and (d_4) are the EDS mapping of Ti, Al, V and C of the selective area in (d), respectively; (e) STEM image of the phase boundary and EDS mapping; (f) Bright-field image of phase boundary; (g) HRTEM image of the selective area in the (f) and SAED pattern obtained by FFT.

Figure 7 illustrates the sintering mechanisms of interfacial structure evolutions between Ti, Al-V, and GNPs. Firstly, due to the high reactivity of C atoms at graphene defects, interfacial TiC formation preferentially occurs at the defect sites of graphene (e.g., their edges, vacancies, nanopores and amorphous carbon), which provide active sites for the TiC formation [21, 38, 54]. The diffusion rate of C atoms at a high temperatures is four orders of magnitude higher than that of Ti atoms [55]. At the initial sintering stage, the C atoms at the defect sites are easily diffused into the adjacent Ti-6Al-4V matrix and react quickly with active Ti atoms to form TiC particles [38]. Secondly, the phase transition generated during sintering is caused by the interdiffusion of Ti, Al, and V elements between the Al-V master alloy and the Ti matrix and the gradual dissolution of the master alloy [56]. Previous studies have shown that Al diffuses much faster than V in Ti matrix [57], resulting in Al-rich and V-rich regions during the sintering process. Finally, the Al-rich and V-rich regions start to show phase transformation over a wide temperature range, resulting in the formation of the lamellar Widmanstatten structure [32].

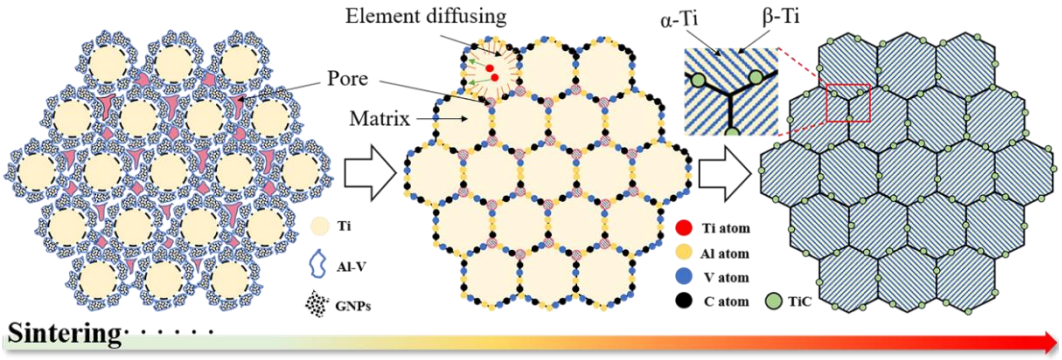

Figure 7. Schematic illustration of the sintering mechanism of Ti-6Al-4V matrix composites.

2.3 Mechanical properties and fracture behaviors

Figure 8a shows the tensile stress-strain curves of the sintered Ti-6Al-4V alloy and composites fabricated using the BEPM method. The YS and UTS obtained from the sintered Ti-6Al-4V alloys are 889.0 MPa and 988.3 MPa, respectively, and the total fracture elongation is still maintained at about 14.2%. The YS and UTS of 0.1 wt.% GNPs/Ti-6Al-4V composite are 1028.4 MPa and 1121.6 MPa, which are increased by 15.7% and 13.5% compared to the Ti-6Al-4V alloy, respectively. However, the ductility of composites is decreased with the increase of GNPs content, and the total fracture elongation of 0.2 wt.% GNPs/Ti-6Al-4V composite is only 4.1%. The strength enhancement effect is strongly related to the formation of TiC during the sintering process, which can effectively transfer the load from the titanium matrix to TiC due to its high strength and hardness. Meanwhile, TiC particles formed at the grain boundary also have a strong suppression of grain growth in the matrix which also benefits the enhancement of strengths for the composites. However, the formation of excessive TiC deteriorates the homogeneity of the Ti-6Al-4V matrix, which is detrimental to its ductility [58]. Moreover, those *in-situ* formed TiC particles and residual graphene hinder the rapid diffusion of Ti atoms, resulting in incomplete formation of sintered

necks at lower temperatures. The formation of these unfinished sintered necks usually results in a significant reduction in the ductility of the composite [21].

The obtained hardness values of the sintered samples are shown in **Figure 8d**. Compared to the pure Ti-6Al-4V alloy, the hardness of 0.2 wt.% GNPs/Ti-6Al-4V composites is increased by ~11.2% (from 311.1 HV to 350.3 HV). As shown in **Figure 8d,** the ultimate tensile strength in this work is relatively higher than most of the other reported Ti-6Al-4V composites reinforced with carbon nanomaterials using various fabrication procedures including selective laser melting, hot isostatic pressing and spark plasma sintering [21, 24, 25, 40, 58-61]. These data reveal that the BEPM and spark plasma sintering used in this study could be a potential method for fabrication of high-performance TMCs.

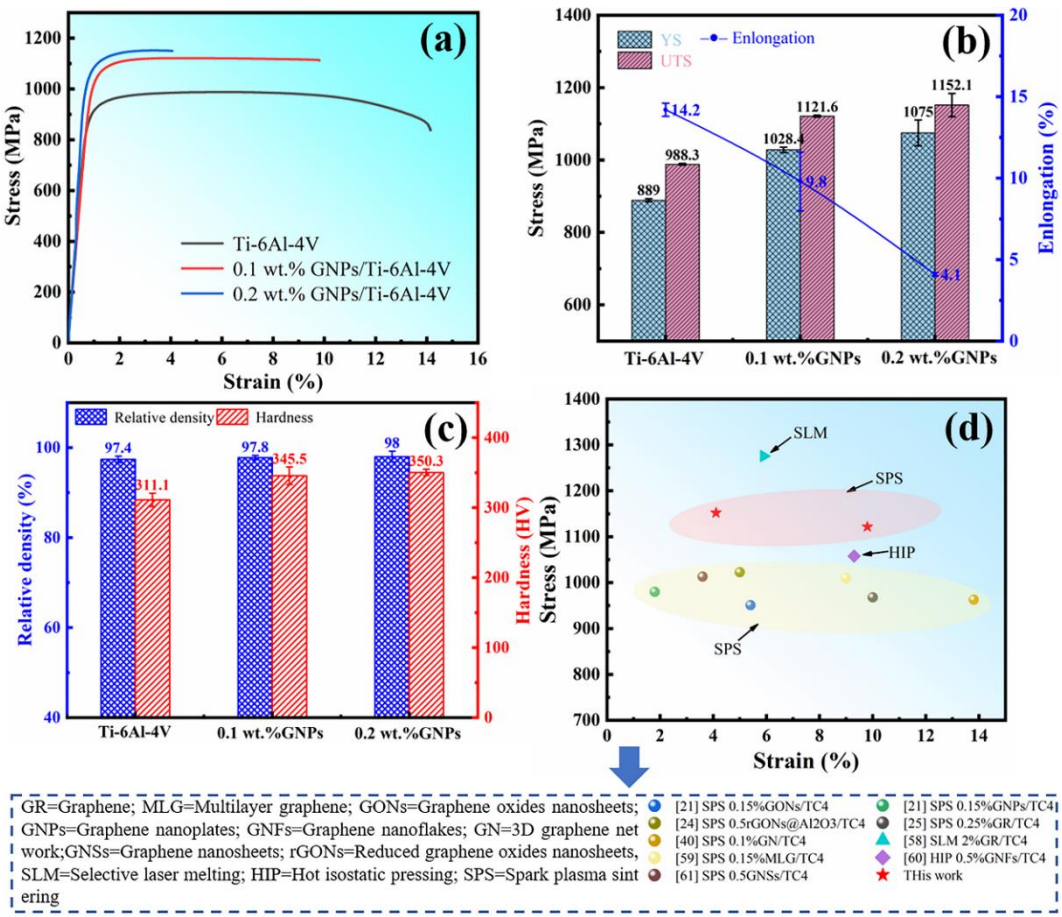

Figure 8. (a) Tensile stress-strain curves of BEPM Ti-6Al-4V alloys and GNPs/Ti-6Al-

4V composites; (b) Corresponding tensile properties of the as-prepared specimens at the room temperature; (c) Relative density and hardness of the as-prepared specimens; (d) Representative tensile properties of graphene/Ti-6Al-4V composites in reported works [21, 24, 25, 40, 58-61].

Figure 9(a) shows that the fracture surface of the sintered Ti-6Al-4V alloy exhibits a typical ductile fracture with many dimples, revealing its good ductility (**Figure 8a**). However, with the addition of GNPs, the number of dimples shown on fracture surfaces of 0.1 wt.% GNPs/Ti-6Al-4V composite is decreased significantly, and cleavage steps can be clearly observed (**Figures 9b** and **9b$_1$**), showing that the fracture mode of the composite is changed from ductile fracture to quasi-cleavage fracture. With the further increase in GNPs content, the fracture surface appears to exhibit a "rock sugar" morphology in **Figures 9(c)** and **9(c$_1$)**. The cracks appear along the boundary of these "rock sugar" features, which clearly indicates the intergranular fracture mechanism of the composition. This fracture occurs at where the brittle TiC particles formed among grains, rather than at the interfaces between TiC and Ti-6Al-4V [40].

In order to further investigate the fracture behavior of GNPs/Ti-6Al-4V composites, morphologies of longitudinal fracture surfaces were observed, and the results obtained are shown in **Figure 10**. Microcracks initiate in the matrix near fracture. As the axial load force increases, the local microcracks begin to spread gradually, causing the material to fracture. On the other hand, GNPs clusters are also detected and observed at the fracture surfaces (**Figure 10b**), which means that these GNPs are also fractured. The results indicate that GNPs could provide a certain load transfer effect during the fracture process. With the increase of graphene content and the axial load force, many TiC particles could easily generate cracks on the fracture surface (**Figure**

10c), and the fractured TiC is still attached to the surface of the matrix, indicating the strong interfacial bonding of GNPs/Ti-6Al-4V. These can significantly enhance the load transfer capability of GNPs/Ti-6Al-4V composites [21].

The strengthening mechanism of GNPs/Ti-6Al-4V composites is mainly due to the formation of *in-situ* TiC particles. The strengthening effects of TiC particles are mainly reflected in the following aspects. Firstly, the pinning effect of TiC particles *in-situ* formed at grain boundaries limits the rapid growth of matrix grains. As a result, the grain is refined, the number of grain boundaries is increased, the dislocation slip is blocked, and the strength of the material is improved. Secondly, TiC particles inhibit the movement of dislocations, leading to an increase in dislocations around TiC, and the aggregation of dislocations may contribute to sustained strain-hardening in GNPs/Ti-6Al-4V composites [51]. Thirdly, as a hard reinforcement, TiC has a significant load transfer effect, which can improve the strength and hardness of GNPs/Ti-6Al-4V composite. While these strengthening mechanisms are generally thought to occur simultaneously [62].

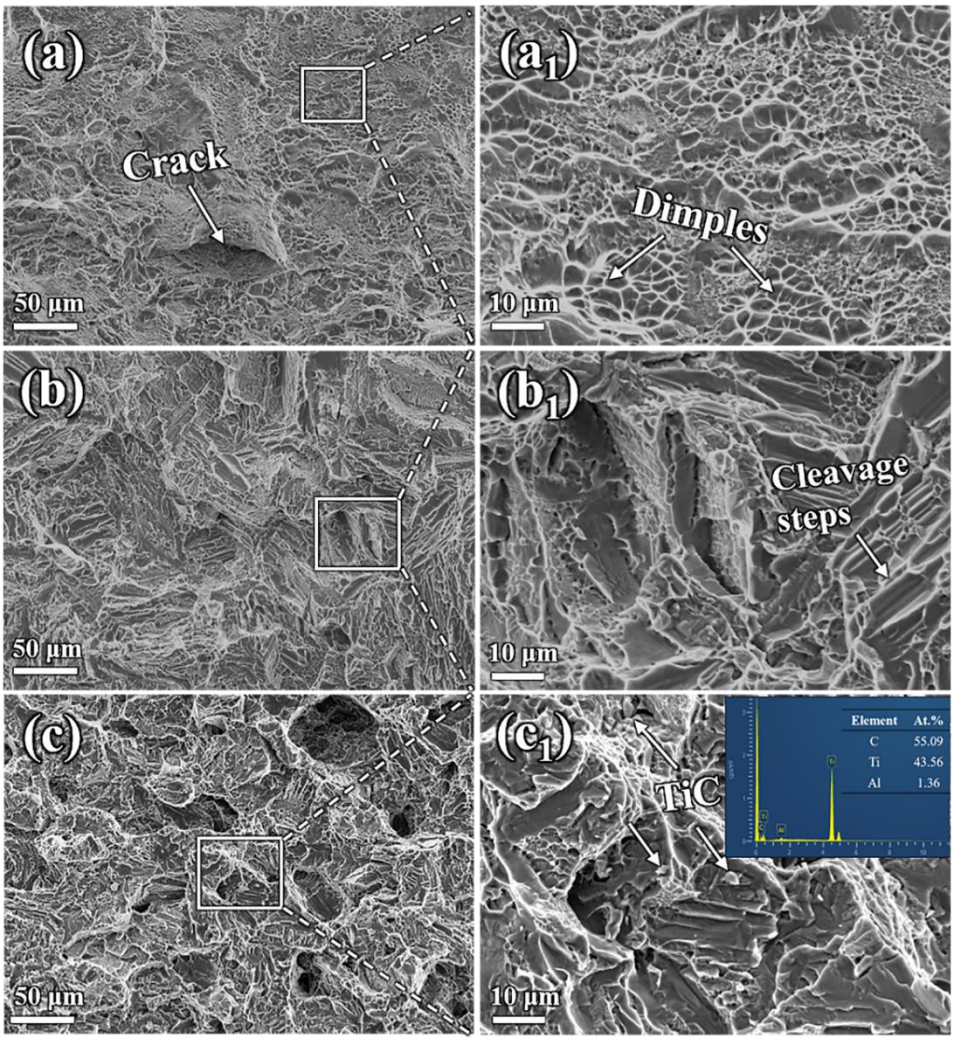

Figure 9. SEM morphologies of fracture surface: (a) Ti-6Al-4V alloy; (b) 0.1 wt.% GNPs/Ti-6Al-4V composite; (c) 0.2 wt.% GNPs/Ti-6Al-4V composite.

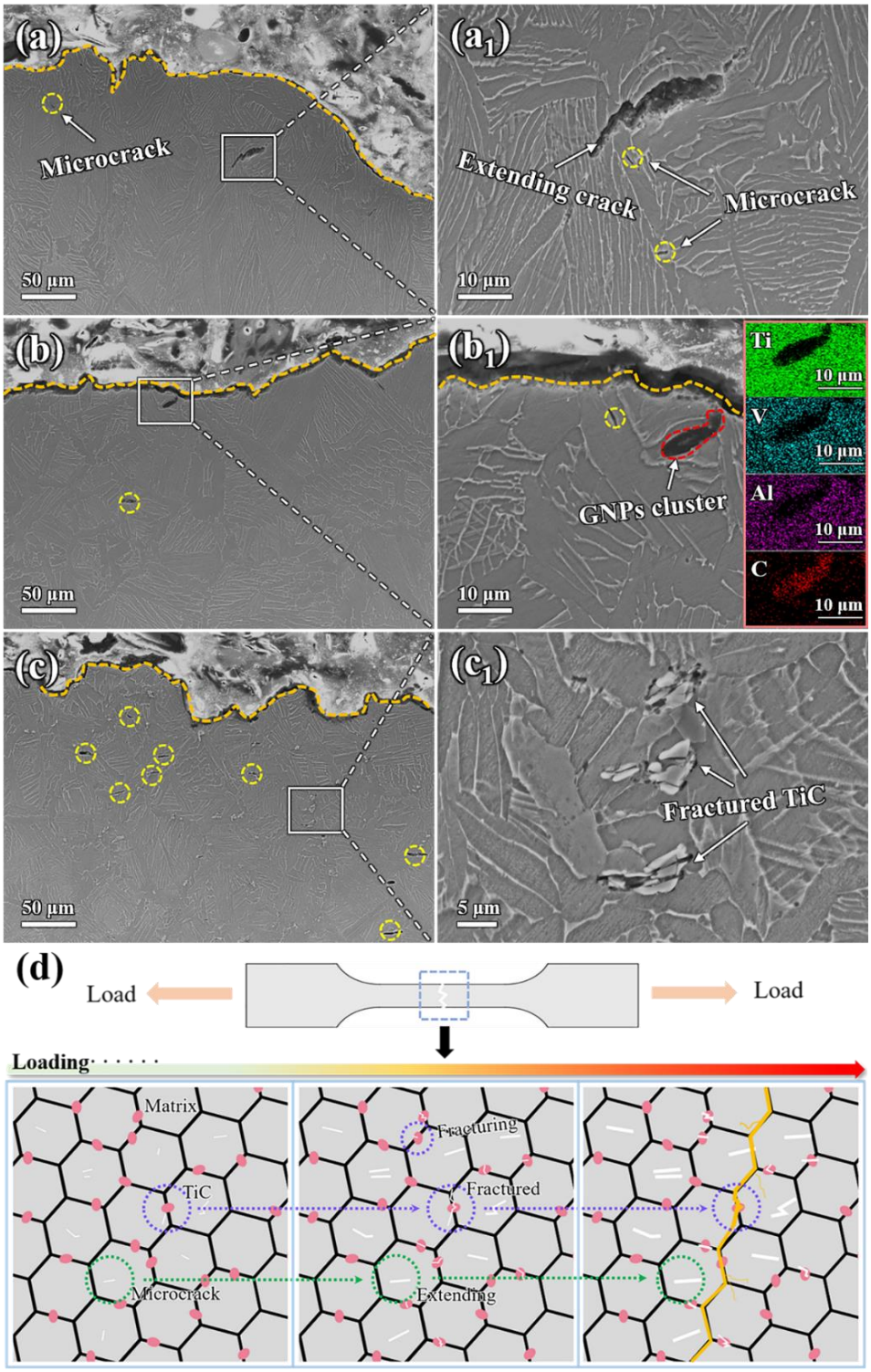

Figure 10. SEM image of the longitudinal fracture section of (a) Ti-6Al-4V alloy、 (b) 0.1 wt.% GNPs/Ti-6Al-4V composite and (c) 0.2 wt.% GNPs/Ti-6Al-4V composite, respectively; (d) Schematic illustration of the fracture mechanism of GNPs/Ti-6Al-4V composites.

4. Conclusions

In summary, Ti-6Al-4V alloy and GNPs/Ti-6Al-4V composites were fabricated using BEPM and SPS processes. Microstructure and mechanical properties of sintered composites were systematically investigated. The main conclusions are:

a) Graphene/Ti-6Al-4V matrix composites microstructures showed a typical Widmanstatten structures without apparent pores and microcracks. Their grain size was significantly refined with the addition of GNPs owing to TiC particles *in-situ* formed restricted Ti grain growth. Graphene induced the precipitation of needle-like nano-secondary phases in trigeminal grain boundary β phases, which strengthened the β-Ti soft phase.

b) The maximum YS and UTS of the sintered Ti-6Al-4V alloy were 889.0 MPa and 988.3 MPa, respectively, and the total fracture elongation was maintained at about 14.2%, whereas GNPs/Ti-6Al-4V exhibited superior strengths (e.g., YS and UTS of 1028.4 and 1121.6 MPa, 14.4% and 13.5% higher than that of matrix) and maintained good ductility of ~ 9.8% with only addition of 0.1 wt.% GNPs.

c) The strengthening mechanisms were mainly attributed to grain refinement, secondary α phases precipitation strength and dislocations strengthening. The fracture mode of the composite was gradually changed from ductile fracture to brittle fracture with the gradual increase of GNPs content.

CRediT authorship contribution statement

Longlong Dong supported and assisted in supervision on the project; **Longlong Dong and Ming Zhu** planned and supervised the project; **Yuanmeng Wang and Hang Xue** performed the experiments; **Guodong Sun and Wei Zhang** analyzed the microstructure characterization and mechanical behaviors; **Yongqing Fu and Ahmed Elmarakbi** involved in the data analysis and discussions; **Longlong Dong and Yusheng Zhang** analyzed data and wrote the manuscript**,** and all the authors modified and corrected the manuscript**.**

Declaration of competing interest

The authors declare that they have no known competing financial interests or personal relationships that could have appeared to influence the work reported in this paper.

Acknowledgments

The authors would like to acknowledge the financial supports from the National Natural Science Foundation of China (NSFC No. 52271138), the Shaanxi Science Foundation For Distinguished Young Scholars (2020JC-50), National Program for Introduction of Foreign Experts (G2022041019L), Key Research and Development Program of Shaanxi Province (2023-YBGY-433, 2021SF-296) and an International Exchange Grant (IEC/NSFC/201078) through the Royal Society and the NSFC.

Reference

[1] V.V. Joshi, C. Lavender, V. Moxon, V. Duz, E. Nyberg, K.S. Weil, Development of Ti-6Al-4V and Ti-1Al-8V-5Fe alloys using low-cost TiH_2 powder feedstock, Journal of Materials Engineering and Performance, 22 (2012) 995-1003.
[2] Y.F. Zheng, X. Yao, Y.J. Su, D.L. Zhang, Fabrication of an in-situ Ti-2.6vol%TiC metal matrix composite by thermomechanical consolidation of a TiH_2-1vol%CNTs powder blend, Materials Science and Engineering: A, 667 (2016) 300-310.
[3] Y.F. Luo, Y.H. Xie, L. Cao, J.M. Liang, Y. Liu, D.L. Zhang, Harmonically structured Ti–6Al–4V alloy with ultrahigh strength fabricated by thermomechanical consolidation of mechanically milled TiH_2/Al60V40 powder blend, Materials Science and Engineering: A, 787 (2020) 139493.
[4] S.L. Wei, L.J. Huang, X.T. Li, Q. An, L. Geng, Interactive effects of cyclic oxidation and structural evolution for Ti-6Al-4V/(TiC+TiB) alloy composites at elevated temperatures, Journal of Alloys and Compounds, 752 (2018) 164-178.
[5] J.L. Zhang, B. Song, C. Cai, L.J. Zhang, Y.S. Shi, Tailorable microstructure and mechanical properties of selective laser melted TiB/Ti–6Al–4V composite by heat treatment, Advanced Powder Materials, 1 (2022) 100010.
[6] G.W. Qiao, B. Zhang, Q. Bai, Y.M. Gao, W. Du, Y.W. Zhang, Machinability of TiC-reinforced titanium matrix composites fabricated by additive manufacturing, Journal of Manufacturing Processes, 76 (2022) 412-418.
[7] H.L. Li, Z.H. Yang, D.L. Cai, D.C. Jia, Y. Zhou, Microstructure evolution and mechanical properties of selective laser melted bulk-form titanium matrix nanocomposites with minor B_4C additions, Materials & Design, 185 (2020) 108245.
[8] U.O. Okoli, I.O. Otunniyi, I.D. Adebiyi, Dry sliding wear behaviour of binary powder laser cladded Ti-6Al-4V using SiC and Al, Materials Today: Proceedings, 38 (2021) 988-993.
[9] M. Selva Kumar, P. Chandrasekar, P. Chandramohan, M. Mohanraj, Characterisation of titanium–titanium boride composites processed by powder metallurgy techniques, Materials Characterization, 73 (2012) 43-51.
[10] S.C. Tjong, Y.W. Mai, Processing-structure-property aspects of particulate- and whisker-reinforced titanium matrix composites, Composites Science and Technology, 68 (2008) 583-601.
[11] Y.H. Guo, K. Yu, J.Z. Niu, M. Sun, G.Q. Dai, Z.G. Sun, H. Chang, Effect of reinforcement content on microstructures and mechanical properties of graphene nanoflakes-reinforced titanium alloy matrix composites, Journal of Materials Research and Technology, 15 (2021) 6871-6882.
[12] X.Q. Liu, C.J. Li, X. You, Z.Y. Xu, X. Li, R. Bao, J.M. Tao, J.H. Yi, Size-dependent effects of Ti powders in the pure aluminum matrix composites reinforced by carbon nanotubes, Journal of Alloys and Compounds, 823 (2020) 153824.
[13] B.K. Jiang, A.Y. Chen, J.F. Gu, J.T. Fan, Y. Liu, P. Wang, H.J. Li, H. Sun, J.H. Yang, X.Y. Wang, Corrosion resistance enhancement of magnesium alloy by N-doped graphene quantum dots and polymethyltrimethoxysilane composite coating, Carbon, 157 (2020) 537-548.
[14] L.L. Dong, Y.Q. Fu, Y. Liu, J.W. Lu, W. Zhang, W.T. Huo, L.H. Jin, Y.S. Zhang, Interface engineering of graphene/copper matrix composites decorated with tungsten

carbide for enhanced physico-mechanical properties, Carbon, 173 (2021) 41-53.
[15] L.L. Dong, B. Xiao, Y. Liu, Y.L. Li, Y.Q. Fu, Y.Q. Zhao, Y.S. Zhang, Sintering effect on microstructural evolution and mechanical properties of spark plasma sintered Ti matrix composites reinforced by reduced graphene oxides, Ceramics International, 44 (2018) 17835-17844.
[16] L.L. Dong, B. Xiao, L.H. Jin, J.W. Lu, Y. Liu, Y.Q. Fu, Y.Q. Zhao, G.H. Wu, Y.S. Zhang, Mechanisms of simultaneously enhanced strength and ductility of titanium matrix composites reinforced with nanosheets of graphene oxides, Ceramics International, 45 (2019) 19370-19379.
[17] L. Liu, Y.K. Li, H.M. Zhang, X.W. Cheng, X.N. Mu, Q.B. Fan, Y.X. Ge, S.D. Guo, Simultaneously enhancing strength and ductility in graphene nanoplatelets reinforced titanium (GNPs/Ti) composites through a novel three-dimensional interface design, Composites Part B: Engineering, 216 (2021) 108851.
[18] W. Zhang, S.Q. Zhou, W.J. Ren, Y.J. Yang, L. Shi, Q.H. Zhou, M.B. Liu, Uniformly dispersing GNPs for fabricating graphene-reinforced pure Ti matrix composites with enhanced strength and ductility, Journal of Alloys and Compounds, 888 (2021) 161527.
[19] Y.X. Ge, H.M. Zhang, X.W. Cheng, Q.B. Fan, Z.H. Zhang, X.N. Mu, L. Liu, Towards high performance in Ti-based composite through manipulating nickel coatings on graphene reinforcement, Journal of Alloys and Compounds, 893 (2022) 162240.
[20] L. Liu, Y.K. Li, H.M. Zhang, X.W. Cheng, X.N. Mu, W. Lei, Enhanced strain-hardening capability in graphene nanoplatelets reinforced Ti composites through tailoring a novel three-dimensional interface structure, Composites Part A: Applied Science and Manufacturing, 156 (2022) 106892.
[21] L.L. Dong, J.W. Lu, Y.Q. Fu, W.T. Huo, Y. Liu, D.D. Li, Y.S. Zhang, Carbonaceous nanomaterial reinforced Ti-6Al-4V matrix composites: properties, interfacial structures and strengthening mechanisms, Carbon, 164 (2020) 272-286.
[22] L.L. Dong, W. Zhang, Y.Q. Fu, J.W. Lu, X.T. Liu, N. Tian, Y.S. Zhang, Reduced graphene oxide nanosheets decorated with copper and silver nanoparticles for achieving superior strength and ductility in titanium composites, ACS Appl Mater Interfaces, 13 (2021) 43197-43208.
[23] N. Tian, L.L. Dong, H.L. Wang, Y.Q. Fu, W.T. Huo, Y. Liu, J.S. Yu, Y.S. Zhang, Microstructure and tribological properties of titanium matrix nanocomposites through powder metallurgy using graphene oxide nanosheets enhanced copper powders and spark plasma sintering, Journal of Alloys and Compounds, 867 (2021) 159093.
[24] H. Xue, M. Zhu, L.L. Dong, W. Zhang, X.C. Sun, Y.M. Wang, Y.Q. Fu, Y.S. Zhang, In-situ synthesis of reduced graphene oxide/aluminium oxide nanopowders for reinforcing Ti-6Al-4V composites, Journal of Alloys and Compounds, 905 (2022) 164198.
[25] F.M. Zhang, J. Wang, T.F. Liu, C.Y. Shang, Enhanced mechanical properties of few-layer graphene reinforced titanium alloy matrix nanocomposites with a network architecture, Materials & Design, 186 (2020) 108330.
[26] W.W. Zhou, K.H. Kamata, M.Q. Dong, N. Nomura, Laser powder bed fusion additive manufacturing, microstructure evolution, and mechanical performance of carbon nanotube-decorated titanium alloy powders, Powder Technology, 382 (2021)

274-283.
[27] M.Q. Dong, W.W. Zhou, Z.X. Zhou, N. Nomura, Simultaneous enhancement of powder properties, additive manufacturability, and mechanical performance of Ti–6Al–4V alloy by 2D-nanocarbon decoration, Materials Science and Engineering: A, 859 (2022) 144215.
[28] H. Attar, S. Ehtemam-Haghighi, D. Kent, M.S. Dargusch, Recent developments and opportunities in additive manufacturing of titanium-based matrix composites: A review, International Journal of Machine Tools and Manufacture, 133 (2018) 85-102.
[29] Q. Yan, B. Chen, J.S. Li, Super-high-strength graphene/titanium composites fabricated by selective laser melting, Carbon, 174 (2021) 451-462.
[30] K.Y. Liu, J.S. Li, J. Wan, Q. Yan, K. Kondoh, J. Shen, S. Li, B. Chen, Sintering-free fabrication of high-strength titanium matrix composites reinforced with carbon nanotubes, Carbon, 197 (2022) 412-424.
[31] Y.P. Dong, Y.L. Li, S.Y. Zhou, Y.H. Zhou, M.S. Dargusch, H.X. Peng, M. Yan, Cost-affordable Ti-6Al-4V for additive manufacturing: powder modification, compositional modulation and laser in-situ alloying, Additive Manufacturing, 37 (2021) 101699.
[32] C. Zhang, F. Yang, C.G. Chen, Z.M. Guo, The microstructure and mechanical properties of extra low interstitials (ELI) Ti-6Al-4V alloys manufactured from hydride–dehydride (HDH) powder, 873 (2021) 159757.
[33] Y.C. Song, G.Y. Ma, F.C. Qiu, O. Stasiuk, D. Savvakin, O. Ivasishin, X.F. Xu, T. Cheng, Nearly dense Ti–6Al–4V/TiB composites manufactured via hydrogen assisted BEPM, Ceramics International, 48 (2022) 10902-10910.
[34] S.Z. Zhang, J.W. Liu, Q.Y. Zhao, C.J. Zhang, L. Bolzoni, F. Yang, Microstructure characterization of a high strength Ti–6Al–4V alloy prepared from a powder mixture of TiH_2 and 60Al40V masteralloy powders, Journal of Alloys and Compounds, 818 (2020) 152815.
[35] F. Yang, B. Gabbitas, Feasibility of producing Ti-6Al-4V alloy for engineering application by powder compact extrusion of blended elemental powder mixtures, Journal of Alloys and Compounds, 695 (2017) 1455-1461.
[36] W. Xu, S.Q. Xiao, X. Lu, G. Chen, C.C. Liu, X.H. Qu, Fabrication of commercial pure Ti by selective laser melting using hydride-dehydride titanium powders treated by ball milling, Journal of Materials Science & Technology, 35 (2019) 322-327.
[37] W.D. Shi, Q. Yan, J.H. Shen, B. Chen, Y.L. Li, Quasi-continuous GNS network induced local dynamic recrystallization along interfaces in titanium MMCs under high strain rate loading, Materials Science and Engineering: A, 852 (2022) 143723.
[38] W.J. Ren, M.B. Liu, W. Zhang, Y.J. Yang, X.H. Wang, S.Q. Zhou, J.X. Du, Microstructure and mechanical behaviour of TiCx-MLG-TiCx network reinforced Ti6Al4V fabricated with core-shell structure powders, Journal of Alloys and Compounds, 897 (2022) 163210.
[39] H.T. Wang, M. Lefler, Z.Z. Fang, T. Lei, S.M. Fang, J.M. Zhang, Q. Zhao, Titanium and titanium alloy via sintering of TiH_2, Key Engineering Materials, 436 (2010) 157-163.
[40] Y.J. Yang, M.B. Liu, S.Q. Zhou, W.J. Ren, Q.H. Zhou, L. Shi, Breaking through

the strength-ductility trade-off in graphene reinforced Ti-6Al-4V composites, Journal of Alloys and Compounds, 871 (2021) 159535.
[41] J.S. Yu, Q.Y. Zhao, Y.Q. Zhao, W. Zhang, L.L. Dong, J.W. Lu, W.T. Huo, Y.S. Zhang, The tribological behavior of different carbon nanomaterials-reinforced the titanium (TC21) matrix composite, Journal of Materials Research and Technology, 15 (2021) 3683-3693.
[42] F. Lin, M.Y. Ren, H. Wu, Y. Lu, M.S. Huo, M. Yang, Z.X. Chen, Z.Y. Jiang, Fabrication of TiC-graphene dual-reinforced self-lubricating Al matrix hybrid nanocomposites with superior mechanical and tribological properties, Tribology International, 171 (2022) 107535.
[43] B. Nayebi, S.A. Delbari, M. Shahedi Asl, E. Ghasali, N. Parvin, M. Shokouhimehr, A nanostructural approach to the interfacial phenomena in spark plasma sintered TiB_2 ceramics with vanadium and graphite additives, Composites Part B: Engineering, 222 (2021) 109069.
[44] J.W. Lu, L.L. Dong, Y. Liu, Y.Q. Fu, W. Zhang, Y. Du, Y.S. Zhang, Y.Q. Zhao, Simultaneously enhancing the strength and ductility in titanium matrix composites via discontinuous network structure, Composites Part A: Applied Science and Manufacturing, 136 (2020) 105971.
[45] Y. Zhou, L.L. Dong, Q.H. Yang, W.T. Huo, Y.Q. Fu, J.S. Yu, Y. Liu, Y.S. Zhang, Controlled interfacial reactions and superior mechanical properties of high energy ball milled/spark plasma sintered Ti–6Al–4V–graphene composite, Advanced Engineering Materials, 23 (2021) 2001411.
[46] X.N. Mu, H.M. Zhang, H.N. Cai, Q.B. Fan, Z.H. Zhang, Y. Wu, Z.J. Fu, D.H. Yu, Microstructure evolution and superior tensile properties of low content graphene nanoplatelets reinforced pure Ti matrix composites, Materials Science and Engineering: A, 687 (2017) 164-174.
[47] J.W. Lu, Y.Q. Zhao, Y. Du, W. Zhang, Y.S. Zhang, Microstructure and mechanical properties of a novel titanium alloy with homogeneous $(TiHf)_5Si_3$ article-reinforcements, Journal of Alloys and Compounds, 778 (2019) 115-123.
[48] J.L. Su, X.K. Ji, J. Liu, J. Teng, F.L. Jiang, D.F. Fu, H. Zhang, Revealing the decomposition mechanisms of dislocations and metastable α' phase and their effects on mechanical properties in a Ti-6Al-4V alloy, Journal of Materials Science & Technology, 107 (2022) 136-148.
[49] P.C. Huo, Z.Y. Zhao, W.B. Du, Z. Zhang, P.K. Bai, D. Tie, Deformation strengthening mechanism of in situ TiC/TC4 alloy nanocomposites produced by selective laser melting, Composites Part B: Engineering, 225 (2021) 109305.
[50] S.R. Huang, H. Wu, H.G. Zhu, Z.H. Xie, J.L. Cheng, Enhanced tensile properties of $CrMnFeCoNi_{0.8}$ high entropy alloy with *in-situ* TiC particles, Intermetallics, 148 (2022) 107639.
[51] N. Xiong, R. Bao, J.H. Yi, D. Fang, J.M. Tao, Y.C. Liu, CNTs/Cu-Ti composites fabrication through the synergistic reinforcement of CNTs and in situ generated nano-TiC particles, Journal of Alloys and Compounds, 770 (2019) 204-213.
[52] W.D. Shi, Q. Yan, J.H. Shen, B. Chen, Y.L. Li, Enhanced adiabatic shear band susceptibility in Ti composites reinforced with quasi-continuous network of graphene

nanosheets, Composites Part A: Applied Science and Manufacturing, 160 (2022) 107055.
[53] J.B. Hou, F.H. Chi, G.R. Cui, W.Z. Chen, W.C. Zhang, Strengthening effects of *in-situ* synthetic nano-TiC particles on Ti64 based nanocomposites through adding graphene nanoplatelets, Vacuum, 177 (2020) 109431.
[54] K. Chu, F. Wang, X.H. Wang, Y.B. Li, Z.R. Geng, D.J. Huang, H. Zhang, Interface design of graphene/copper composites by matrix alloying with titanium, Materials & Design, 144 (2018) 290-303.
[55] A. Miriyev, M. Sinder, N. Frage, Thermal stability and growth kinetics of the interfacial TiC layer in the Ti alloy/carbon steel system, Acta Materialia, 75 (2014) 348-355.
[56] G. Steedman, S.F. Corbin, Determining sintering mechanisms and rate of *in-situ* homogenisation during master alloy sintering of Ti-6Al-4V, Powder Metallurgy, 58 (2014) 67-80.
[57] A. Carman, L.C. Zhang, O.M. Ivasishin, D.G. Savvakin, M.V. Matviychuk, E.V. Pereloma, Role of alloying elements in microstructure evolution and alloying elements behaviour during sintering of a near-β titanium alloy, Materials Science and Engineering: A, 528 (2011) 1686-1693.
[58] C.Y. Shang, F.M. Zhang, B. Zhang, F. Chen, Interface microstructure and strengthening mechanisms of multilayer graphene reinforced titanium alloy matrix nanocomposites with network architectures, Materials & Design, 196 (2020) 109119.
[59] K.J. Lin, Y.M. Fang, D.D. Gu, Q. Ge, J. Zhuang, L.X. Xi, Selective laser melting of graphene reinforced titanium matrix composites: powder preparation and its formability, Advanced Powder Technology, 32 (2021) 1426-1437.
[60] Z. Cao, X.D. Wang, J.L. Li, Y. Wu, H.P. Zhang, J.Q. Guo, S.Q. Wang, Reinforcement with graphene nanoflakes in titanium matrix composites, Journal of Alloys and Compounds, 696 (2017) 498-502.
[61] Q. Yan, B. Chen, L. Cao, K.Y. Liu, S. Li, L. Jia, K. Kondoh, J.S. Li, Improved mechanical properties in titanium matrix composites reinforced with quasi-continuously networked graphene nanosheets and in-situ formed carbides, Journal of Materials Science & Technology, 96 (2022) 85-93.
[62] K. Chu, F. Wang, Y.B. Li, X.H. Wang, D.J. Huang, H. Zhang, Interface structure and strengthening behavior of graphene/CuCr composites, Carbon, 133 (2018) 127-139.